CANUCS: UV and ionizing properties of dwarf star-forming galaxies at z ~ 5–7

Harshan, Anishya; Bradač, Maruša; Abraham, Roberto; Asada, Yoshihisa; Brammer, Gabriel; Desprez, Guillaume; Iyer, Karthiek; Martis, Nicholas S; Matharu, Jasleen; Mowla, Lamiya; Muzzin, Adam; Noirot, Gaël; Rihtaršič, Gregor; Sarrouh, Ghassan T E; Sawicki, Marcin; Strait, Victoria; Willott, Chris J

Publisher's version / Version de l'éditeur:
https://doi.org/10.1093/mnras/stae1574
Monthly Notices of the Royal Astronomical Society, 532, 1, pp. 1112-1125, 2024-06-25

Monthly Notices of the ROYAL ASTRONOMICAL SOCIETY

MNRAS **532,** 1112–1125 (2024) https://doi.org/10.1093/mnras/stae1574
Advance Access publication 2024 June 25

CANUCS: UV and ionizing properties of dwarf star-forming galaxies at $z \sim 5$–7

Anishya Harshan [1]★ Maruša Bradač [1] Roberto Abraham [2,3] Yoshihisa Asada [4,5] Gabriel Brammer [6] Guillaume Desprez [4] Karthiek Iyer [7] Nicholas S. Martis [1,4,8] Jasleen Matharu [6,9] Lamiya Mowla [10] Adam Muzzin,[11] Gaël Noirot,[4] Gregor Rihtaršič [1] Ghassan T. E. Sarrouh [11] Marcin Sawicki [4] Victoria Strait [6,9] and Chris J. Willott [8]

[1]*University of Ljubljana, Department of Mathematics and Physics, Jadranska ulica 19, SI-1000 Ljubljana, Slovenia*
[2]*David A. Dunlap Department of Astronomy and Astrophysics, University of Toronto, 50 St. George Street, Toronto, ON M5S 3H4, Canada*
[3]*Dunlap Institute for Astronomy and Astrophysics, 50 St. George Street, Toronto, ON M5S 3H4, Canada*
[4]*Department of Astronomy and Physics, Institute for Computational Astrophysics, Saint Mary's University, 923 Robie Street, Halifax, NS B3H 3C3, Canada*
[5]*Department of Astronomy, Kyoto University, Sakyo-ku, Kyoto 606-8502, Japan*
[6]*Niels Bohr Institute, University of Copenhagen, Jagtvej 128, DK-2200 Copenhagen N, Denmark*
[7]*Columbia Astrophysics Laboratory, Columbia University, 550 West 120th Street, New York, NY 10027, USA*
[8]*National Research Council of Canada, Herzberg Astronomy and Astrophysics Research Centre, 5071 West Saanich Road, Victoria, BC V9E 2E7, Canada*
[9]*Cosmic Dawn Center (DAWN), Denmark*
[10]*Whitin Observatory, Department of Physics and Astronomy, Wellesley College, 106 Central Street, Wellesley, MA 02481, USA*
[11]*Department of Physics and Astronomy, York University, 4700 Keele St. Toronto, ON M3J 1P3, Canada*

Accepted 2024 June 13. Received 2024 June 1; in original form 2023 September 30

ABSTRACT

The epoch of reionization (EoR) progressed through the emission of ionizing photons from galaxies to their local intergalactic medium. In this work, we characterize the dwarf star-forming galaxies as candidates for the source of ionizing photons that drove EoR. We investigate the ionizing properties and star formation histories of star-forming dwarf galaxies at the last stages of EoR at $4.8 < z < 7$ using observations from the CAnadian NIRISS Unbiased Cluster Survey (CANUCS). The magnification due to gravitational lensing allows us to probe large dynamic ranges in stellar mass ($2 \times 10^6 \leq M_*/\mathrm{M}_\odot \leq 5 \times 10^9$) and ultraviolet (UV) magnitudes ($-22.68 \leq M_{\mathrm{UV}} \leq= -15.95$). We find a median UV slope β_{1500} of -2.56 ± 0.23 and the production efficiency of ionizing photons $\log\xi_{\mathrm{ion}} = 25.39 \pm 0.6$ for the full sample ($4.8 < z < 7$) with a median stellar mass of $6.3 \pm 0.5 \times 10^7$ $\mathrm{M}_\odot$. We find both β_{1500} and ξ_{ion} are marginally correlated with the stellar mass of the galaxy, indicating a possible greater contribution of dwarf galaxies to the reionization of the Universe. We find that on average, galaxies in our sample are experiencing a recent rise/burst of star formation which translates to a higher scatter in ξ_{ion} and a large scatter in Hα equivalent widths (EWs). Finally, we investigate the trends of Hα and [O III] + Hβ EWs with UV magnitude and find M_{UV} is correlated between Hα but not with [O III] + Hβ EWs indicating low metallicities and recent burst in the UV faint galaxies.

Key words: galaxies: evolution – galaxies: high-redshift – dark ages, reionization, first stars.

1 INTRODUCTION

The production of ionizing photons is a fundamental process that plays a crucial role in shaping the reionization history of the Universe. However, the sources of ionizing photons that drove reionization at redshifts $z > 5.5$ (e.g. McGreer, Mesinger & D'Odorico 2015; Davies et al. 2018; Bolan et al. 2022) are poorly understood. Current observational evidence suggests that reionization proceeded through the escape of ionizing photons from young massive stellar populations in galaxies (see review Robertson 2022, and references within). To ascertain the contribution of different galaxies to reionization, we need to determine the rate of ionizing photons emitted into the intergalactic medium (IGM) from different galaxy populations. The rate of ionizing photons emitted by galaxies can be determined by combining the non-ionizing ultraviolet (UV) luminosity function, escape fraction of ionizing photons into the IGM and the ionizing photon production efficiency.

The ionizing photon production efficiency (ξ_{ion}) is the measure of rate of hydrogen-ionizing photon production ($E \geq 13.6$ eV) by young massive stars in a galaxy per unit non-ionizing UV continuum luminosity produced on average by the less massive stars. Thus, ξ_{ion} should depend on the fraction of massive ionizing stars which is regulated by the initial mass function (IMF) and the star formation history (SFH) of the galaxy. Along with the escape fraction of ionizing photons (f_{esc}), ξ_{ion} is used to determine whether a galaxy is capable of reionizing the local IGM. Direct measurement of ξ_{ion} requires detection of ionizing Ly-continuum photons emitted by

★ E-mail:anishya.thevalil-harshan@fmf.uni-lj.si

the galaxy which becomes increasingly difficult for high-redshift galaxies as the radiation would be absorbed by the IGM. Thus, the measurement of $\xi_{\rm ion}$ for high-redshift galaxies has exclusively relied on indirect methods. As the bright nebular recombination line Hα (6562 Å) is directly related to the total number of Ly-continuum photons produced by stars in a galaxy (assuming an escape fraction of zero: Leitherer & Heckman 1995), Hα line can be used to constrain $\xi_{\rm ion}$ (e.g. Bouwens et al. 2016; Chisholm et al. 2022; Stefanon et al. 2022; Prieto-Lyon et al. 2023).

The past decade has seen many studies estimating $\xi_{\rm ion}$ using indirect Hα at $z\sim$ 4–5 based on stacking *Spitzer*/Infrared Array Camera photometry (e.g. Bouwens et al. 2016; Lam et al. 2019; Stefanon et al. 2019) and at lower redshifts $z\sim$ 1–3.7, where Hα or Hβ was observable from ground-based telescopes (Nakajima et al. 2016; Nanayakkara et al. 2020; Matthee et al. 2017). These studies indicate that the $\xi_{\rm ion}$ increases with redshift, and thus the average escape fraction required for galaxies to ionize the local IGM would be $\approx$ 10 per cent–20 per cent (Ouchi et al. 2009; Robertson et al. 2015; Finkelstein et al. 2019; Naidu et al. 2020) at $z = 6$. However, most studies relied on low statistics, lower redshift analogues or wide-band photometry and image stacking due to lack of access to Balmer lines. This has been mitigated with the launch of the *JWST*, and we are able to observe Balmer lines using spectroscopy and/or medium/narrow-band photometry to accurately measure Hα fluxes. Recently a number of studies using *JWST* observations like Lin et al. (2023), Simmonds et al. (2023), Tang et al. (2023), Saxena et al. (2023), Prieto-Lyon et al. (2023), Atek et al. (2023), and Mascia et al. (2023) have measured $\xi_{\rm ion}$, however, these studies rely on luminous and/or high-mass galaxies or small samples for dwarf galaxies. Thus, the ionization properties of faint, low-mass galaxies remain unclear.

Observational studies suggest that low-mass galaxies should have a high contribution to the reionization of the Universe because of their abundance indicated by the steep slope at the faint end of the UV luminosity function in the high-redshift Universe (Sawicki & Thompson 2006; Reddy & Steidel 2009; Bouwens et al. 2012; Dressler et al. 2015; Finkelstein et al. 2015; Ishigaki et al. 2015; Livermore, Finkelstein & Lotz 2017; Mehta et al. 2017; Atek et al. 2018; Bhatawdekar et al. 2019; Atek et al. 2023). The same is also suggested by simulation studies like Balu et al. (2023), who suggest that inclusion of low-mass haloes significantly increases the progression of reionization. Additionally, owing to the low gravitational potential along with stochastic SFHs, low stellar mass galaxies are thought to have a higher escape fraction of ionizing photons into the local IGM (Paardekooper, Khochfar & Vecchia 2013; Wise et al. 2014; Erb 2015; Anderson et al. 2017; Karman et al. 2017) at high redshifts. In order to determine the contribution of low-mass galaxies to the reionization of the Universe, we need to investigate their star formation and ionizing properties and compare them to their massive counterparts. However, due to the faintness of low-mass galaxies, most studies have focused on more massive and luminous galaxies.

To that end, we use the CAnadian NIRISS Unbiased Cluster Survey (CANUCS, Willott et al. 2022), to study the low-mass galaxies at redshift $z>$ 5. The magnification provided by the lensing galaxy clusters along with the capabilities of the *JWST* means we are now able to spectroscopically observe low stellar mass faint galaxies that were previously hidden at $z>$ 5. With CANUCS, we are able to reach UV magnitude $M_{\rm UV} \approx -15.95$ compared to $M_{\rm UV} \approx -16.4$ from the deep imaging from the JWST Advanced Deep Extragalactic Survey (JADES; Eisenstein et al. 2023; Endsley et al. 2023a) for galaxies at $6 < z < 9$. We use medium- and broad-band photometry from JWST/NIRCam and prism spectroscopy from JWST/NIRSpec to study the ionization properties and SFHs of star-forming galaxies at $5 < z < 7$. The outline of the paper is as follows: we describe the observations, data reduction, and sample selection in Section 2. In Section 3, we describe the methodology followed for flux measurements from photometric and spectroscopic observations, dust correction, and measurements of UV and ionizing properties. In Section 4, we discuss the results on the UV slope, $\xi_{\rm ion}$, and emission-line equivalent widths (EWs), and finally summarize our findings in Section 5.

We assume a flat lambda-cold dark matter cosmology with $\Omega_m = 0.3$, $\Omega_\Lambda = 0.7$, h = 0.7, all magnitudes are in the AB system.

2 DATA AND TARGET SELECTION

2.1 Imaging data

In this work, we use data from the CANUCS (Willott et al. 2022), a *JWST* GTO program (program ID 1208; PI: C.Willott) and the *HST* (*Hubble Space Telescope*) program 16667 (PI: M. Bradac). We select our sample from the observations of the MACS J0417.5−1154 cluster (CLU) field and the respective NIRCam flanking (NCF) field. In the central CLU field, the CANUCS imaging data consist of *HST*/ACS filters: *F435W*, *F606W*, and *F814W* and *JWST*/NIRCam filters: *F090W*, *F115W*, *F150W*, *F200W*, *F277W*, *F356W*, *F410M*, and *F444W*. In the NCF field, we have *HST*/WFC3 filters: *F438M* and *F606W* and *JWST*/NIRCam filters: *F090W*, *F115W*, *F140M*, *F150W*, *F162M*, *F182M*, *F210M*, *F250M*, *F277W*, *F300M*, *F335M*, *F360M*, *F410M*, and *F444W*. CANUCS image reduction and photometry procedure is described in detail in Noirot et al. (2023). In short, we use a modified version of the Detector1Pipeline (calwebb_detector1) stage of the official STScI pipeline and jwst_0916.pmap JWST Operational Pipeline (CRDS_CTX) to reduce the NIRCam data. We perform astrometric alignment of the different exposures of *JWST*/NIRCam to *HST*/ACS images, sky subtraction, and drizzling to a common pixel scale of 0.04 arcsec using version 1.6.0 of the grism redshift and line analysis software for space-based spectroscopy (Grizli Brammer & Matharu 2021). The source detection and photometry is done with the PHOTUTILS package (Bradley et al. 2022) on the $\chi_{\rm mean}$ detection image created using all available images. For each detected source, total fluxes are measured in elliptical apertures based on the Kron radius and circular apertures of diameter 0.3 and 0.7 arcsec (Asada et al. 2024). In this work, we use 0.7 − arcsec-diameter aperture photometry on *HST*/ACS and *JWST*/NIRCam images that were point spread function homogenized to the resolution of the *F444W* data (Sarrouh et al., in preparation). We calculate the photometric redshifts using EAZY-PY (Brammer, van Dokkum & Coppi 2008; Brammer 2023a) with spectral energy distribution (SED) templates from Larson et al. (2022) that are based on FSPS (Flexible Stellar Population Synthesis, Conroy & Gunn 2010) and BPASS (Eldridge et al. 2017) stellar population synthesis models and CLOUDY (Ferland et al. 2017; Byler 2018) photoionization code.

We select our photometric sample between redshift 4.8 and 5.5 such that the medium-band *F410M* of *JWST*/NIRCam includes flux from the Hα (6562 Å) emission line creating a flux excess. We get a sample of 270 objects with flux excess in *F410M* (i.e. $\rm Flux_{F410M} > Flux_{F444W}$) in the selected redshift range. We impose a signal-to-noise ratio (SNR) cut for Lyman-break dropout ($\rm SNR_{F606W} < 2$ and $\rm SNR_{F090W} > 3$) and visually inspect each object and select our final sample of 156 galaxies. We refer to this sample as the NIRCam sample throughout the paper.

2.2 Spectroscopic data

Galaxies selected with excess flux in *F410M* and Lyman-break dropout in *F606W*, *F814W* or *F090W* were selected for spectroscopic follow-up without imposing a magnitude limit with *JWST*/NIRSpec microshutter assembly in the low-resolution Prism mode. Our NIRSpec data have been reduced using the *JWST* pipeline for stage 1 corrections and then the msaexp (Brammer 2023b) to create wavelength calibrated, background-subtracted 2D spectra. The 1D spectrum is then created for each line by collapsing the spectrum in the spatial axis and extracting the 1D spectrum within 3σ of the peak of the collapsed spectrum. From the CANUCS spectroscopic observations, we confirm a sample of 33 galaxies with Hα emission line at $4.8 < z < 7$.

The wavelength coverage of the NIRSpec prism allows for observation of Hα emission at $4.8 < z < 7$. Thus, our NIRSpec data cover a higher redshift range compared to our NIRCam sample which covers $4.8 < z < 5.5$. The NIRCam data are limited in wavelength to allow for accurate measurement of Hα flux, which can be achieved when Hα emission falls in the *F410M* band (in $4.8 < z < 5.5$). The lower observational depth of the spectroscopic data compared to the NIRCam imaging leads to a sample of lower magnification uncorrected $M_{\rm UV}$ of -24.37 to -18.45 with median $M_{\rm UV} = -20.95 \pm 1.15$ in our NIRSpec Sample compared to uncorrected the $M_{\rm UV}$ range of -23.13 to -18.10 with median $M_{\rm UV} = -20.56 \pm 0.85$ in our NIRCam Sample. Similarly, the magnification uncorrected stellar masses of the NIRSpec sample is in the range $7.78 < \log M_*/{\rm M}_\odot < 9.51$ with a median $\log M_*/{\rm M}_\odot = 8.11 \pm 0.42$ compared to the $\log M_*/{\rm M}_\odot$ range $7.67 < \log M_*/{\rm M}_\odot < 9.75$ with a median $\log M_*/{\rm M}_\odot = 8.04 \pm 0.38$ for the NIRCam sample. The properties of the two sample sets are presented in Table 1 and shown in Fig. 1.

3 METHODS

3.1 SED fitting and flux measurements

We calculate the photometric redshifts using EAZY-PY (Brammer et al. 2008; Brammer 2023a) including SED templates from Larson et al. (2022) that are better suited to fit the SEDs of blue high-redshift ($5 < z < 8$) galaxies. We used Dense Basis (Iyer & Gawiser 2017; Iyer et al. 2019) SED fitting code to determine other physical properties of galaxies: stellar masses, star formation rates (SFRs), metallicities, stellar dust attenuation and non-parametric SFHs. Dense Basis uses FSPS code (Conroy & Gunn 2010) which includes a prescription for nebular emission from CLOUDY (Ferland et al. 2017; Byler 2018). We adopt the Calzetti et al. (2000) dust model and assume Chabrier (2003) IMF. We fit the photometry from 3 *HST*/ACS bands and 8 *JWST*/NIRCam bands covering a wavelength range of 0.4–4 μm for the CLU field and 2 *HST*/WFC3 bands and 14 *JWST*/NIRCam bands for the NCF field covering a wavelength range of 0.4–4 μm. The photometric sample is selected with Hα flux excess in the *F410M* medium band and has been visually inspected to be a Lyman-continuum dropout in the *F606W* or *F814W* bands. Thus, we run Dense Basis with uniform redshift prior in $4.7 < z < 6$ range. For the spectroscopic sample, we fix the redshift at the measured spectroscopic redshift, while running Dense Basis. We use flat stellar mass prior between $5 < \log M_*/{\rm M}_\odot < 12$, flat specific SFR (sSFR) prior between $-12 <$ sSFR $(yr^{-1}) < -7$, varied metallicity in the range $-2.5 < \log(Z/Z_\odot) < 0.25$ and used an exponential prior for dust attenuation. We then correct the stellar mass, SFR, and SFHs for magnification from gravitational lensing from the foreground cluster. The magnification coefficients are calculated using an updated lens model for MACS0417 (Desprez, in preparation) created with LENSTOOL (Kneib et al. 1993; Jullo et al. 2007). The model improves upon the Mahler et al. (2019) model by adding several new spectroscopically confirmed multiply imaged systems.

Fig. 1 shows the stellar mass distributions before and after magnification corrections. Our sample shows (not corrected for magnification) a lower limit of $\log M_*/{\rm M}_\odot = 7.3$ (orange unfilled histogram, left) for the NIRCam sample and $\log M_*/{\rm M}_\odot = 7.78$ (purple unfilled histogram, left) for the NIRSpec sample. After correcting for magnification from gravitational lensing from the cluster, the stellar mass sample ranges between $6.36 < \log M_*/{\rm M}_\odot < 9.76$ with median $\log M_*/{\rm M}_\odot = 7.88 \pm 0.57$ and $6.69 < \log M_*/{\rm M}_\odot < 9.21$ with median $\log M_*/{\rm M}_\odot = 7.94 \pm 0.53$ for the NIRCam and NIRSpec samples, respectively, shown in filled histograms in Fig. 1. In our sample, the median lensing magnification is 3 ± 1. Given the distance of the NCF field from the cluster centre, we assume a magnification of 1.

We measure the Hα flux from the photometry by following the two-filter method and the three-filter method described in Vilella-Rojo et al. (2015) for the CLU and NCF field, respectively. In the CLU field, we use the *F444W* broad-band filter to describe the stellar continuum and the *F410M* medium band with flux excess from Hα ($4.8 < z < 5.5$). In the NCF field, we calculate the continuum with the *F360M* medium-band filter and the *F444W* broad-band filter and use the *F410M* medium band that contains the Hα flux. Similarly, only in the NCF field, we calculate the [O III] + Hβ flux for the NIRCam sample using the *F300M*, *F335M*, and *F360M* bands. We do not calculate the [O III] + Hβ flux for galaxies in the CLU field as the [O III] + Hβ falls in the *F277W* and *F356W* broad bands for the NIRCam sample which would include spectral features like [O II], Balmer break, etc. We calculate the rest-frame EW for each emission-line measurement using the extracted emission line following Vilella-Rojo et al. (2015). We bootstrap the photometry within the photometric errors and measure the line fluxes and rest-frame EWs. We take the median values and 1σ of the distribution as the measured line flux and EWs and associated errors.

For our NIRSpec data, we use the ID spectra and correct for slit loss by performing a spline interpolation of the ratio of mock photometry from the 1D spectrum and the observed photometry and smoothing the interpolated function. For the spline interpolation, we also ignored the photometric bands where the mock photometry from the NIRSpec spectrum was less than 2 SNR. We then extract the 1D spectrum in 200 Å wavelength windows around emission lines Hα, [O III], and Hβ and subtract the local continuum if present. Fluxes and accurate redshifts are then calculated by fitting Gaussian curves on the emission line without putting constraints on the width of the Gaussian. We bootstrap the spectrum with the error spectrum and calculate fluxes. The median flux and redshift and the 1σ of the distribution of the bootstrap are taken as the measured values and associated errors. Given the low resolution of the spectroscopic data from the NIRSpec prism, we note that the Hα emission may have contamination from [N II](6585 Å) emission, and the [O III] (5007,4959 Å) doublet is not always fully resolved (depending on SNR). Cameron et al. (2023) found no significant observation of [N II] in deep observation of Lyman-break galaxies in $z \sim 5.5 - 9.5$. Thus, we assume a negligible contribution of [N II] to the measured Hα flux. We follow a similar assumption while calculating Hα flux from the medium-band photometry. However, we note that if we are to assume ≈ 10 per cent contribution of [N II] as is observed

Table 1. Summary of median values and ranges (in parentheses) of physical properties of the NIRCam and NIRSpec sample. Stellar mass ($\log M_*/M_\odot$) and UV magnitude (M_{UV}) are corrected for magnification.

Sample	z	$\log M_*/M_\odot$	M_{UV}	β_{1500}	ξ_{ion}
NIRCam	5.15 ± 0.2 (4.8–5.5)	7.8 ± 0.5 (6.3–9.7)	-20.0 ± 1.2 (-22.7 to -15.9)	-2.58 ± 0.2 (-3.15 to -0.83)	25.36 ± 0.04 (24.26–26.37)
NIRSpec	5.5 ± 0.6 (4.8–7)	7.9 ± 0.5 (6.7–9.2)	-20.1 ± 1.2 (-21.8 to 17.0)	-2.48 ± 0.4 (-2.78 to -1.73)	25.48 ± 1.0 (21.25–26.75)

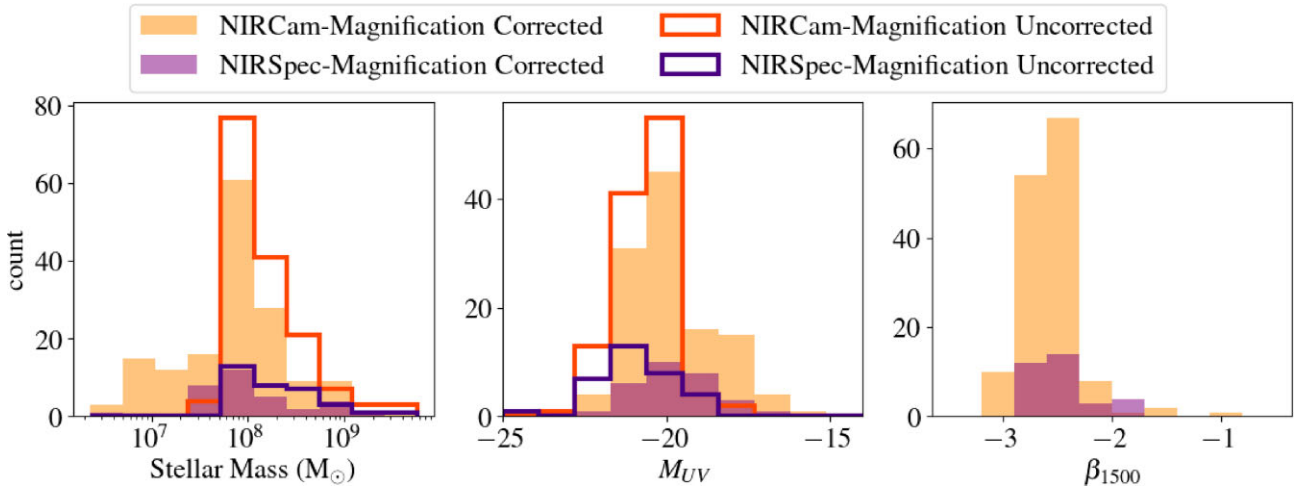

Figure 1. Distribution of stellar mass (left), UV magnitude in AB system (centre) and the UV slope at 1500 Å (right) for our selected sample. The orange histograms represent the NIRCam sample at redshift $4.8 > z > 5.5$, and the violet histograms represent the NIRSpec sample at $4.8 > z > 7$. The filled and unfilled histograms represent the magnification corrected and uncorrected quantities, respectively. Gravitational lensing correction improves our detection limits by 1 dex in $\log M_*/M_\odot$ and 2.1 dex in M_{UV} .

at $z \sim 2$ (Coil et al. 2015; Alcorn et al. 2019), our Hα fluxes and quantities measured with Hα fluxes will be lowered by ≈ 10 per cent. Fig. 2 shows reasonable agreement (< 7 per cent difference) between the Hα flux measured with photometric data versus spectroscopy. We note that this comparison has been done within the overlapping NIRCam + NIRSpec sample (at $4.8 < z < 5.5$).

3.2 UV luminosity and UV continuum slope

We measure the UV luminosity of galaxies in the NIRCam sample using filters covering rest-frame 1400–1600 Å. Thus, we use *F090W* for galaxies between the redshift range of 4.8–5.5 which avoids the Lyman-break and Lyman-α emission. For the spectroscopic sample, we use the slit loss corrected 1D spectrum and calculate the UV luminosity in the wavelength window containing 1500 Å determined by the *F090W* or *F115W* for each object depending on the redshift. We correct the measured UV luminosity for both photometric and spectroscopic data for lensing magnification. Finally, we bootstrap the measurements within observational errors and report the median values and 1σ errors. Fig. 2 compares the UV luminosity measured using photometric and spectroscopic data. We find reasonable agreement between the UV luminosity measured with the two methods with the relative difference being 0.11 ± 0.45.

We calculate β_{1500} from the model SED from EAZY SED fitting of the observed photometry. We measure β_{1500} by fitting model SED between rest-frame 1400–2000 Å with a single power law in the wavelength windows defined by Calzetti, Kinney & Storchi-Bergmann (1994) to avoid absorption and emission lines. β_{1500} measured with EAZY SED fitting is highly dependent on the templates. The inclusion of the Larson et al. (2022) improves the measurement of β_{1500} by increasing the range to reach up to $\beta_{1500} = -3.1$.

Fig. 1 shows the UV magnitude and β_{1500} distributions before and after magnification corrections. Our sample shows a lower limit (before magnification correction) of $M_{UV} = -18.1$ (orange unfilled histogram, centre) for the NIRCam sample and $M_{UV} = -18.45$ (purple unfilled histogram, centre) for the NIRSpec sample. After correcting for magnification from lensing from the cluster, the UV magnitude ranges between $-22.68 < M_{UV} < -15.95$ with median $M_{UV} = -20.07 \pm 1.27$ and $-21.7 < M_{UV} < -17.01$ with median $M_{UV} = -20.1 \pm 1.17$ for the NIRCam and NIRSpec samples, respectively (filled histograms in Fig. 1, centre). Given the achromatic nature of lensing, β_{1500} is not affected by lensing magnification. The distribution of β_{1500} shows a median $\beta_{1500} = -2.58 \pm 0.26$ for the NIRCam sample and a median $\beta_{1500} = -2.48 \pm 0.42$ in the NIRSpec sample. After Fig. 1, we only present magnification corrected quantities.

3.3 Dust correction

The measured Hα fluxes are corrected for nebular dust attenuation to account for the light absorbed by dust in the star-forming regions in the galaxy. The Balmer decrement (Hα/Hβ) is one of the most robust ways to correct for nebular dust attenuation. To calculate the intrinsic Hα luminosity for our spectroscopic sample, we determine the dust attenuation towards Hα by calculating the Balmer colour excess following the Case B recombination value (Osterbrock 1989)

$$E\,(\mathrm{H}\beta - \mathrm{H}\alpha) = 2.5 \log\left(\frac{\mathrm{H}\alpha/\mathrm{H}\beta}{2.86}\right).$$

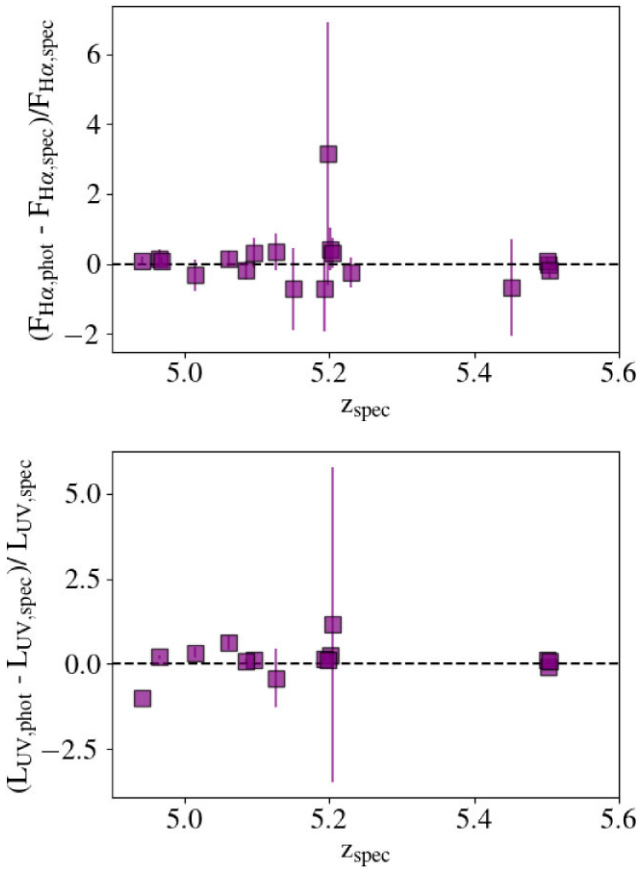

Figure 2. Comparison of Hα flux (top), and UV luminosity (bottom) measured from photometry and spectroscopic data. Our photometric measurements of Hα flux (from *F410M*) and L_{UV} (from *F090W*) are consistent with the spectroscopic measurements.

Following the Calzetti dust law (Calzetti et al. 2000), the intrinsic Hα luminosity is determined as:

$$L_{H\alpha,int} = 10^{0.4A(H\alpha)} \times L_{H\alpha,obs}$$
$$A(H\alpha) = 6.6 \log\left(\frac{H\alpha/H\beta}{2.86}\right).$$

For our photometric sample, where we do not have measurements of Hβ flux to determine the balmer decrement, we use the total attenuation (A_v) determined using Dense Basis SED fitting to calculate the attenuation towards Hα luminosity. For our sample, we calculate the median $A_v = 0.11^{+0.04}_{-0.06}$. We adopt the Calzetti dust law following the recent results from Markov et al. (2024), who find the dust law for galaxies at $z > 4.5$ is comparable to the Calzetti dust law. Following Calzetti dust law (Calzetti et al. 2000), attenuation towards Hα is determined as:

$$A(H\alpha) = 0.82 \times A_v.$$

Given the dust attenuation is higher in the UV wavelengths, the observed UV luminosity in both photometric and spectroscopic data is similarly corrected to determine the intrinsic UV luminosity using the Calzetti dust law at $\lambda = 1500$ Å as:

$$A(1500) = 2.55 \times A_v.$$

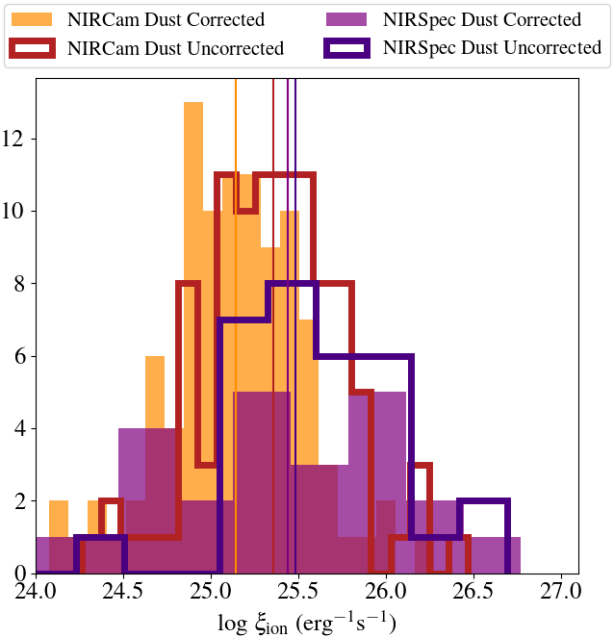

Figure 3. The distribution of ξ_{ion} corrected and uncorrected for dust obscuration is shown in unfilled and filled histograms, respectively. The dust correction follows Calzetti et al. (2000) dust law for the NIRCam sample (orange) and using Balmer decrement in the NIRSpec sample (purple). The NIRSpec sample shows no significant difference in the median of the distribution, but a slight increase in the σ of the distribution. The NIRCam sample shows a lower median ξ_{ion} in the dust corrected sample by ~ 0.2 dex.

3.4 ξ_{ion} measurement

Lyman-continuum photon production efficiency in the presence of a non-zero $f_{esc,LyC}$ is used to determine the contribution of an object in ionizing the IGM. Since the precise value of $f_{esc,LyC}$ is uncertain, we assume a $f_{esc,LyC} = 0$. From indirect measurements of f_{esc}, studies find median predicted $f_{esc,LyC)} < 0.2$ at $6 < z < 9$ (Mascia et al. 2023; Saxena et al. 2023).

Leitherer & Heckman (1995) found the following relation between the Hα luminosity and the intrinsic Lyman-continuum photons production rate computed for dust free Case B recombination (Osterbrock 1989) assuming no escape of ionizing photons:

$$L(H\alpha)\left[\mathrm{erg\,s^{-1}}\right] = 1.36 \times 10^{-12} \dot{N}_{(H_0)}\left[\mathrm{s^{-1}}\right].$$

Thus, we express $\xi_{ion\,0}$ as the ratio of the Lyman-continuum photons production rate to the intrinsic rest-frame UV luminosity (L_{UV}) as:

$$\xi_{ion,0} = \frac{\dot{N}_{(H_0)}}{L_{UV}}.$$

We show the distribution of dust corrected and uncorrected logξ_{ion} for the NIRCam and NIRSpec samples in Fig. 3. We find that for our NIRCam sample on average, dust corrected ξ_{ion} is 0.20 dex lower than the uncorrected ξ_{ion}. We note that for this sample we do not have information on the Balmer decrement. In our NIRSpec sample, for which we have the Balmer decrement, the dust corrected ξ_{ion} is < 0.1 dex higher than the uncorrected ξ_{ion}. Similarly, if we assume Small Magellanic Cloud-like dust attenuation, dust corrected ξ_{ion} is 0.2 and 0.1 dex lower in the NIRCam and NIRSpec samples, respectively. Due to the lack of significant effect of dust on the median ξ_{ion}, we report the dust uncorrected ξ_{ion} in the paper.

4 RESULTS

4.1 The UV slope

The UV continuum slope (β_{1500}) of a galaxy traces the light emitted by young massive stars thus is crucial to constrain the stellar population and SFH of a galaxy. β_{1500} is dependent on the ages, metallicities, and dust content in a galaxy (Duncan & Conselice 2015; Reddy et al. 2018). Given its dependence on the dust content of the galaxy, β_{1500} is often used to constrain the dust attenuation of the spectrum where Balmer decrement or infrared spectrum is not observed. However, intrinsically, for a dust-corrected spectrum, the β_{1500} is dependent on the fraction of very young and metal-poor stellar population. Specifically, young and metal-poor stellar populations result in bluer β_{1500} compared to older metal-rich stellar populations. Given that the main source of ionizing UV radiation in a star forming galaxy is from the young massive stellar population, the production efficiency of ionizing UV radiation ($\xi_{\rm ion}$) is expected to correlate with the β_{1500}. In this section, we study the distribution and the evolution of β_{1500} with galaxy properties.

In Section 3.2, we describe the method we have adopted to measure β_{1500} for the NIRCam samples. In Fig. 1, we present the distribution of β_{1500} with 156 galaxies in the photometric (orange). We find $-3.15 < \beta_{1500} < -0.83$ with the median at $\beta_{1500} = -2.56 \pm 0.26$ in the photometric sample. In Fig. 4, we plot β_{1500} as a function of redshift, stellar mass, and $M_{\rm UV}$ for both the NIRCam (orange) and NIRSpec (purple) samples. The binned sample along with the linear regression between β_{1500} and redshift, stellar mass, and $M_{\rm UV}$ are also shown.

Redshift evolution of $\boldsymbol{\beta_{1500}}$. We find no significant evolution of β_{1500} with the redshift in the NIRCam sample (slope: 0.12, Spearman Coefficient: 0.10). However, we note that our NIRCam sample is restricted to a short range of redshift between $4.8 < z < 5.5$. In our NIRSpec sample, the linear regression measures a slope of 0.07 with a large scatter. Thus, we do not find a significant correlation between β_{1500} and z. This overall trend is comparable to the results in the literature (Bouwens et al. 2015a; Jiang et al. 2020; Nanayakkara et al. 2023; Topping et al. 2023). We note a large scatter in our sample and a lower correlation compared to the empirical relation of β_{1500} with redshift shown by Bouwens et al. (2015a). We also note that previous studies like Jiang et al. (2020) are unable to recover $\beta_{1500} < -2.6$ with SED fitting due to the limitations of the then available templates, whereas β_{1500} calculated using broad-band photometry at high redshift (Bouwens et al. 2015a) are affected by the uncertainties in redshifts as well as spectral features.

Correlation of $\boldsymbol{\beta_{1500}}$ *with stellar mass.* In the middle panel of Fig. 4, we present the correlation of β_{1500} with the stellar mass of the galaxy. The stellar mass (magnification corrected) in our NIRCam sample ranges from $\log M_*/{\rm M}_\odot = 6.3$ to 9.75. We find a moderate correlation of β_{1500} with the magnification corrected stellar mass of the galaxies in both our NIRCam sample such that β_{1500} gets shallower with increasing stellar mass. The linear regression of β_{1500} with stellar mass for the NIRCam sample gives a slope of 0.19 and a Spearman coefficient of 0.46, and a slope of 0.007 with low significance in the NIRSpec sample. In the NIRCam sample, the lower mass sample of $\log M_*/{\rm M}_\odot < 8$ (median $= 7.76 \pm 0.04$) has a $\beta_{1500} = -2.62 \pm 0.02$ compared to $\beta_{1500} = -2.46 \pm 0.04$ in the higher mass sample $\log M_*/{\rm M}_\odot \geq 8$ (median $= 8.26 \pm 0.05$). The bluer β_{1500} of low-mass galaxies implies that the low-mass galaxies could have lower dust content, possible higher fraction of ionizing radiation, or lower metallicities compared to high-mass galaxies. Bluer β_{1500} is also associated with high escape fraction (Chisholm et al. 2022; Mascia et al. 2023), indicating a higher escape fraction in low-mass galaxies and thus a higher contribution of low stellar mass galaxies during the epoch of reionization (EoR). This result is comparable to Nanayakkara et al. (2023) who found a correlation between β_{1500} and the stellar mass of galaxies at $4 < z < 8$ similar to our NIRCam sample. We also note that the β_{1500} calculated in Nanayakkara et al. (2023) follows a similar procedure to measure β_{1500} as our NIRCam sample but they do not perform magnification correction for the stellar mass.

Correlation of $\boldsymbol{\beta_{1500}}$ *with UV magnitude.* Finally, we present the correlation of UV magnitude to the β_{1500} in the right panel in Fig. 4. For our sample with UV magnitude $M_{\rm UV} < -19$, we find a median $\beta_{1500} = -2.58 \pm 0.02$ and for the fainter sample $M_{\rm UV} > -19$, we median find $\beta_{1500} = -2.54 \pm 0.02$. In our NIRCam sample, we do not observe a significant UV magnitude evolution of the β_{1500} (with slope $= -0.01$ and the Spearman coefficient $= -0.02$). Similarly, in the NIRSpec sample, we do not observe a significant UV magnitude evolution of the β_{1500} -with slope $= 0.05$ and Spearman coefficient $= 0.03$.

We find correlation presented in Nanayakkara et al. (2023) and Bouwens et al. (2015a) for a sample at z= 4–7, and Topping et al. (2023) for a sample at z= 5–7 comparable to our NIRCam sample, albeit with a shallower slope of the linear fit. The binned median β_{1500} in Nanayakkara et al. (2023) from the GLASS *JWST* survey at a given UV magnitude is higher compared to our NIRCam sample. However, this discrepancy could be explained by the photometric redshift selection of galaxies in Nanayakkara et al. (2023), whereas we have an additional condition of *F410M* flux excess from Hα emission which biases our sample towards actively star-forming galaxies. Similarly, Topping et al. (2023), who calculate β_{1500} directly from photometry also have higher median β_{1500} values at UV magnitude $M_{\rm UV} < -19$ which could be driven by the Lyman-break selection. However, previous studies like Yamanaka & Yamada (2019) find an opposite correlation between β_{1500} and $M_{\rm UV}$ in the range $(-22 > M_{\rm UV} > -20)$ at $z\sim$ 4. The Lyman-break-selected galaxies in Yamanaka & Yamada (2019) are possibly biased towards higher dust content.

4.2 Ionizing photon production efficiency $\xi_{\rm ion}$

Constraining $\xi_{\rm ion}$ during the EoR for different galaxy populations is important to understand the contribution of different galaxies to EoR and to understand how the reionization of the Universe proceeded. In this section, we explore the evolution of $\xi_{\rm ion}$ with redshift and other galaxy properties at $z\sim$ 4.8–7 in our NIRCam and NIRSpec samples.

4.2.1 *Evolution of* $\xi_{\rm ion}$

We calculate the median $\xi_{\rm ion}$ of Hα selected NIRCam sample in the redshift range $4.8 < z < 5.5 \log \xi_{\rm ion} = 25.36 \pm 0.40$ compared to the NIRSpec sample in the same redshift range with $\log \xi_{\rm ion} = 25.42 \pm 0.3$. In this redshift range, we find comparable results (within 1σ) between our NIRCam and NIRSpec samples. Whereas, the median $\xi_{\rm ion}$ for galaxies in the NIRSpec sample in redshift range $5.5 < z < 7$ is $\log \xi_{\rm ion} = 25.5 \pm 0.2$ which is higher than the median $\xi_{\rm ion}$ at $4.8 < z < 5.5$ by $< 1\sigma$.

In Fig. 5, we put in context our measurements by comparing with Hα emitters at $4 < z < 4.5$ from Faisst et al. (2019), Lyman-break galaxies at $4 < z < 6$ from Bouwens et al. (2016), [O III] emitters at $5 < z < 9$ from Matthee et al. (2023), Tang et al. (2023), and Mascia et al. (2023, also Hα and Ly α emitters), and Lyman-alpha

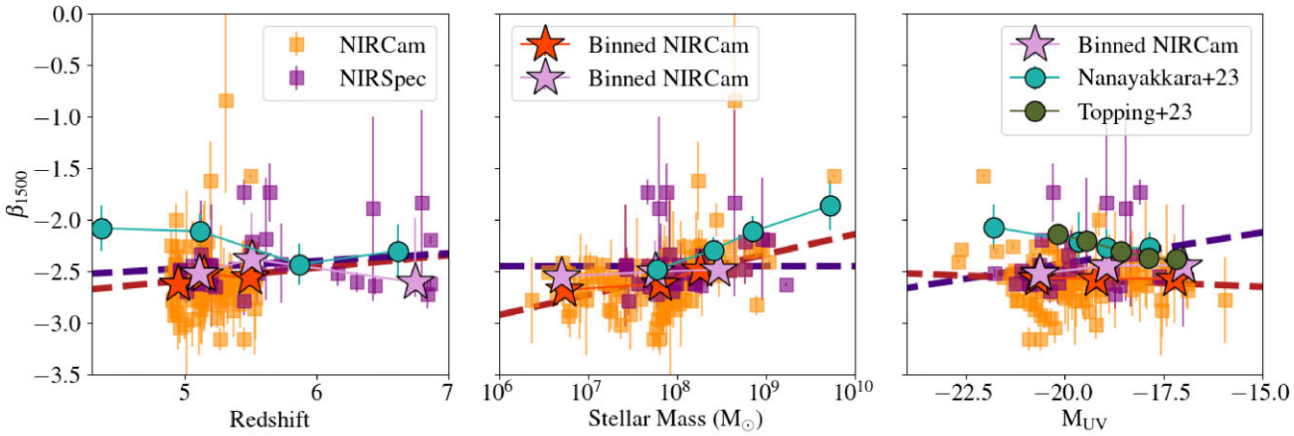

Figure 4. UV continuum slope (β_{1500}) versus redshift (left), stellar mass (centre), and M_{UV} (right). Stars show the binned sample and the dashed lines show the linear fit to the full sample. Within the uncertainties, we find no significant correlation between β_{1500} and redshift or M_{UV} . However, we do find a moderate correlation between the β_{1500} and stellar mass in our samples.

emitters (LAEs) at $z > 4$ from Lam et al. (2019), Ning et al. (2023), Simmonds et al. (2023), and Saxena et al. (2023). Among these, Matthee et al. (2023), Tang et al. (2023), and Saxena et al. (2023) measure Balmer line fluxes directly from spectroscopy and Bouwens et al. (2016), Faisst et al. (2019), Lam et al. (2019), Ning et al. (2023), and Simmonds et al. (2023) make measurements from photometry.

The median $\log \xi_{ion} = 25.36 \pm 0.04$ at $4.8 < z < 5.5$ in our photometric sample is comparable to the median $\log\xi_{ion} = 25.27 \pm 0.03$, 25.5, 25.36 ± 0.08 reported in Bouwens et al. (2016), Faisst et al. (2019), and Lam et al. (2019) at similar redshifts. At $z \sim 6$, ξ_{ion} from Ning et al. (2023) and Simmonds et al. (2023, median $\log\xi_{ion} = 25.48 \pm 0.4$ and $25.44^{+0.21}_{-0.15}$, respectively) are also comparable to our ξ_{ion} at $z < 5.5$. At $5.5 < z < 7$, the median $\log\xi_{ion}$ of $= 25.6 \pm 0.2$ in our NIRSpec sample is comparable to $\log \xi_{ion} = 25.3$, 25.8 ± 0.09 and 25.56 at $6 < z < 8$ reported in Matthee et al. (2023), Tang et al. (2023), and Saxena et al. (2023).

From our NIRSpec sample, we confirm that 4 out of 33 galaxies are LAE with median $\log\xi_{ion} = 25.49 \pm 0.17$ compared to the median $\log \xi_{ion}$ $25.48 = \pm 0.2$ of the non-LAE. We find no significant difference between the ξ_{ion} of LAE and non-LAE in our NIRSpec sample. We also find no significant difference between LAE reported in Lam et al. (2019), Ning et al. (2023), Simmonds et al. (2023), and Saxena et al. (2023) and the non-LAE in our sample. The lack of significant difference between ξ_{ion} in the LAE and non-LAE also indicates different physical processes driving the production of ionizing photons and creating channels of escape for Lyman-α photons in different galaxies similar to the findings in Saxena et al. (2023).

Overall, we find marginal evolution of median ξ_{ion} between our sample and median ξ_{ion} reported in the literature between $4 < z < 9$. At $z < 5.5$. Median $\log \xi_{ion} = 25.36 \pm 0.04$ and $\log \xi_{ion} = 25.48 \pm 1$ for our NIRCam and NIRSpec samples, respectively, is lower ($< 1\sigma$) than 25.8 ± 0.09 and 25.56 reported in Tang et al. (2023) and Saxena et al. (2023). However, it is consistent with $\log \xi_{ion} = 25.36 \pm 0.07$ and 25.3 in Mascia et al. (2023) and Matthee et al. (2023), respectively. We note that the selection of Hα emitters for our sample biases the sample towards higher ξ_{ion} compared to an Lyman break galaxy (LBG) selection that is done in the stated literature studies and we might miss galaxies with low ξ_{ion} . We also find a large scatter in ξ_{ion} , especially in the NIRCam sample, which indicates a stochastic star formation in galaxies at $z > 5$.

4.2.2 ξ_{ion} *versus stellar mass and star formation*

The dependence of the production of ionizing photons on the young and massive stellar population in a galaxy indicates that ξ_{ion} should show a correlation with the stellar mass and the SFH of a galaxy. In this section, we explore the evolution of ξ_{ion} with the stellar mass and SFH of the galaxies.

Fig. 6 shows ξ_{ion} as a function of magnification-corrected stellar mass and the sSFRs calculated from Dense Basis SED fitting of the NIRCam (orange squares) and NIRSpec sample (purple squares). The NIRCam sample covers a range of magnification corrected $\log M_*/M_\odot = 6.3 - 9.8$ and the NIRSpec sample covers the range of $\log M_*/M_\odot = 7.2 - 9.1$. We further bin the sample into five stellar mass bins of $\log M_*/M_\odot = 6.3 - 7$, $7 - 7.5$, $7.5 - 8$, $8 - 8.5$, and > 8.5. The stars show the median ξ_{ion} and the median stellar mass of the binned sample. We find that ξ_{ion} decreases marginally (by ~ 0.12 dex) with increasing stellar mass such that the median $\log \xi_{ion} = 25.57 \pm 0.06$ for galaxies with $\log M_*/M_\odot < 7$ and $= 25.46 \pm 0.1$ for $\log M_*/M_\odot > 8$. The linear fit also shows a negative slope -0.16 and -0.28 for the NIRCam and NIRSpec samples-, respectively. Although the negative slopes indicate a moderate negative correlation between ξ_{ion} and the stellar mass of the galaxy, we note that the intrinsic scatter of the ξ_{ion} measurement is large at standard deviation $1\sigma = 0.40$ for the NIRCam sample and $1\sigma = 1.03$ for the NIRSpec sample. Further, we calculate the Spearman correlation coefficient. We find a negative correlation coefficient of -0.03 for the NIRCam sample and -0.21 for the NIRSpec sample. Our NIRSpec sample indicates a slight negative correlation of ξ_{ion} with the stellar mass of the galaxies within a large intrinsic scatter, however, the Spearman correlation finds no significant correlation between ξ_{ion} and stellar mass in our NIRCam sample.

Given the difficulty in observing faint low stellar mass galaxies at $z \gtrsim 5$, which has only recently been made available with the launch of *JWST*, similar results have been reported in the literature albeit at lower redshifts. Lam et al. (2019) and Castellano et al. (2023) find similar slopes of the linear fit for the correlation between ξ_{ion} and stellar mass at $\log M_*/M_\odot > 7$ and > 8 at redshift ~ 5, respectively. Compared to this sample, we can extend the range of stellar mass by > 1 dex towards the lower mass end. The marginal elevation ξ_{ion} of the lower mass galaxies has important implications for the progression of ionization and the sources of ionizing photons during

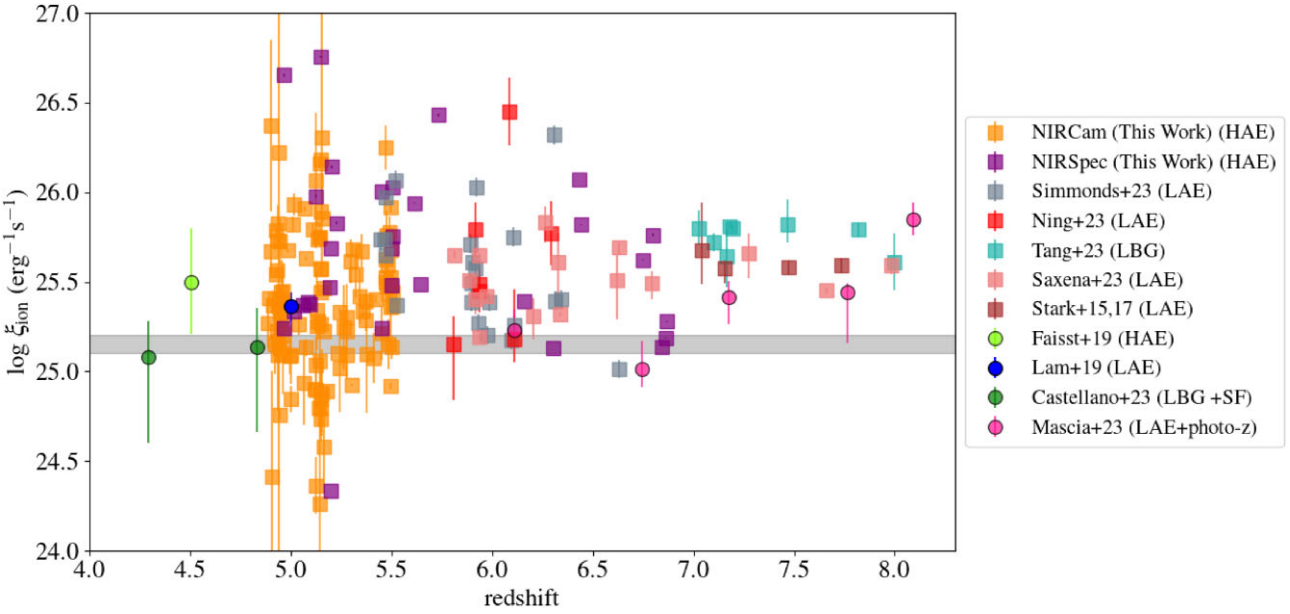

Figure 5. Evolution of the ionizing photon production efficiency $\xi_{\rm ion}$ (uncorrected for dust) with redshift in the EoR. The purple and orange squares of NIRSpec and NIRCam selected samples, respectively, are shown with various measurements of $\xi_{\rm ion}$ from the literature. The method of target selection is mentioned in parentheses. Circles show binned measurements of log$\xi_{\rm ion}$, whereas squares show individual galaxy measurements. The grey line shows the linear fit to the canonical value of $\xi_{\rm ion}$ required to ionize the local IGM as calculated by Robertson et al. (2015). There is no significant evolution of $\xi_{\rm ion}$ during the EoR and the $\xi_{\rm ion}$ of our sample at $z < 5.5$ is comparable to their higher redshift counterparts from the literature within the errors.

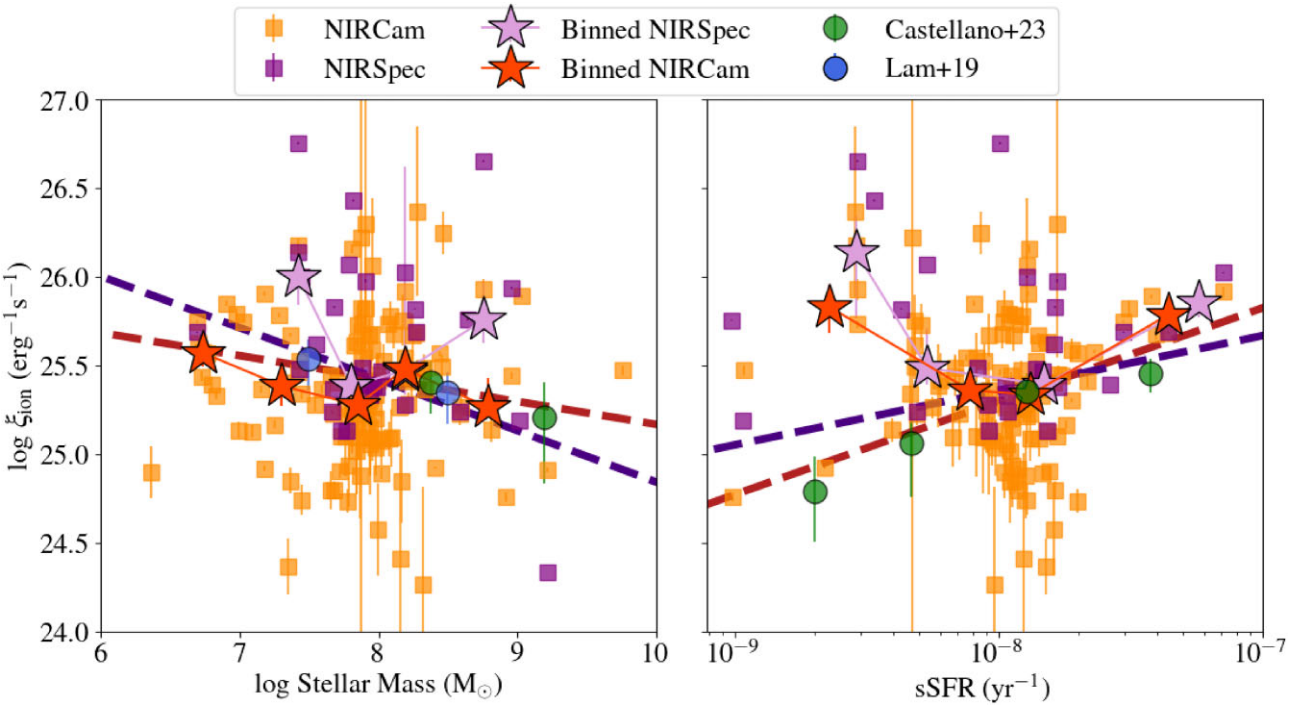

Figure 6. The ionizing photon production efficiency ($\xi_{\rm ion}$) as a function of stellar mass (left) and the sSFR (right). The purple and orange colors show our NIRSpec and NIRCam samples, respectively. The squares and stars show individual galaxies and binned samples with the lines showing linear fits to the sample. We find a moderate negative correlation of $\xi_{\rm ion}$ with the stellar mass of galaxies and a moderate positive correlation of $\xi_{\rm ion}$ with the sSFR. Dwarf star-forming galaxies have a higher photon production efficiency and will require a lower escape fraction to ionize their local IGM.

the EoR. The steep slope of the faint end of the UV luminosity function at $z > 5$ (Bouwens et al. 2015b; Livermore et al. 2017; Atek et al. 2018, 2023) coupled with higher $\xi_{\rm ion}$ of low-mass galaxies indicate such dwarf systems may emit significant ionizing photons into the IGM to reionize their local environment depending on their escape fraction of ionizing photons. However, we note that our sample which is biased towards high $\xi_{\rm ion}$ galaxies especially at

the magnification uncorrected low stellar mass end due to the Hα selection could be driving this difference.

In the right panel of Fig. 6, we show $\xi_{\rm ion}$ as a function of the sSFRs of the galaxies as measured from SED fitting (refer to Section 3.1 for the description of SED fitting). We note that both $\xi_{\rm ion}$ and sSFR are not affected by magnification correction. Our samples cover a range of log sSFR $= -9$ to -7 yr^{-1}. Similar to the stellar mass, we have binned the sample in sSFR and the stars depict the median $\xi_{\rm ion}$ versus the median sSFR of the binned sample. We bin the sample with log sSFR $= -9$ to -8.5, -8.5 to -8, -8 to -7.5, and > -7.5yr^{-1}. In both the NIRCam and NIRSpec samples, we find a positive correlation between $\xi_{\rm ion}$ and sSFR with slope of the linear fit 0.48 for the NIRCam sample and 0.29 for the NIRSpec sample. However, we also find a small subsample of outliers to this correlation at the low sSFR end (log sSFR < 8.5yr^{-1}). This low sSFR end of our sample (~ 10 per cent of the sample) shows a larger scatter and higher median $\xi_{\rm ion}$. This difference could be a result of the Hα selection, which would bias our sample to higher $\xi_{\rm ion}$, especially at low sSFR. We note that between log sSFR -8.5 to -7.5, where ~ 85 per cent of the sample lies, we find no significant correlation of $\xi_{\rm ion}$ -, but a large intrinsic scatter of $\sigma = 0.38$. We further calculate the Spearman coefficient of -0.06 and -0.13 for correlation between $\xi_{\rm ion}$ and log sSFR for the NIRCam and the NIRSpec samples, respectively. Although the linear fit and the Spearman coefficient point towards a slight positive correlation between $\xi_{\rm ion}$ and the sSFR of a galaxy, we note that these results have high intrinsic scatter and do not show a clear correlation.

We compare our results with Castellano et al. (2023), who find a very significant monotonically increasing correlation between $\xi_{\rm ion}$ and sSFR of galaxies at $2 < z < 5$. They report that the $\xi_{\rm ion}$ increases from log$\xi_{\rm ion} = 24.5$Hz erg^{-1} at log sSFR $= -9.5$ yr^{-1} to $= 25.5$Hz erg^{-1} at log sSFR $= -7.5$ yr^{-1}. They also found a Spearman correlation coefficient of ~ 0.79 compared to 0.013 and a large p-value of 0.5 in our sample. Similar to our results, Castellano et al. (2023) also find a larger scatter of $\xi_{\rm ion}$ at the lower end of sSFR indicating a lower correlation of $\xi_{\rm ion}$ with sSFR at the low sSFR end, however, unlike our result, the median $\xi_{\rm ion}$ at the lower sSFR is lower than $\xi_{\rm ion}$ at the higher sSFR end. The difference in the results could be driven by the Hα selection or could also be explained by the redshift evolution of the median sSFR of the galaxies indicating that at $z > 5$, $\xi_{\rm ion}$ is not highly correlated to the sSFR of the galaxy as galaxies may have a stochastic SFH which will rapidly fluctuate the sSFR of a galaxy.

Given the possible effect of stochasticity, we explore further the time-scales with which $\xi_{\rm ion}$ changes with the star formation by studying the correlation of $\xi_{\rm ion}$ with stellar ages and SFHs. We derive the times when the galaxy creates 50 per cent and 75 per cent of its stellar mass (T_{50} and T_{75}, at the time of observation) using the non-parametric histories of Dense Basis SED fitting. Fig. 7 shows $\xi_{\rm ion}$ as a function of the ratio T_{75}/T_{50} (left panel) with each galaxy coloured by its stellar mass. The ratio T_{75}/T_{50} is indicative of the relative time of the last burst of star formation in the galaxy such that a lower T_{75}/T_{50} indicates a more recent burst. We find a moderate positive correlation between $\xi_{\rm ion}$ and $T_{50}/T_{75} < 0.3$ such that $\xi_{\rm ion}$ is decreasing on average with more recent bursts. However, we find a small sample of galaxies with $T_{50}/T_{75} > 0.3$ that have a lower median $\xi_{\rm ion}$. This indicates a potential correlation of $\xi_{\rm ion}$ with the age of the starburst, however, we note that the effect is also dependent on the SFH and the strength of the starburst. We also find the lowest stellar mass galaxies have had a more recent burst compared to the more massive galaxies in our sample. We note that the Hα selection biases our sample to galaxies with ongoing active star formation, that is, either to a rising or bursty SFH.

We further divide our sample into $\xi_{\rm ion}$ bins and plot their median SFHs (right panel, Fig. 7). The median $\xi_{\rm ion}$ of each bin and their respective medians magnification corrected stellar masses are: log$\xi_{\rm ion} = 24.86 \pm 0.05$, 25.28 ± 0.02, 25.69 ± 0.02, and 26.21 ± 0.04 and log $M_*/{\rm M}_\odot = 7.78 \pm 0.14$, 7.89 ± 0.07, 7.88 ± 0.1, and 7.90 ± 0.12. We find that on average our sample is experiencing an ongoing star formation burst. However, this could be a result of the selection of Hα emitters exclusively. The bin with the highest $\xi_{\rm ion}$ started the burst < 100 Myr earlier than the lowest $\xi_{\rm ion}$ bin. Thus, we infer that there may be a potential delay of increase in the production rate of ionizing photons from the start of the last rise in star formation.

4.2.3 $\xi_{\rm ion}$ *versus UV properties*

In this section, we study the correlation of UV properties with $\xi_{\rm ion}$. In Fig. 8, we show $\xi_{\rm ion}$ as a function of the UV slope (β_{1500} , left panel) and the UV magnitude ($M_{\rm UV}$, right panel). We find that $\xi_{\rm ion}$ correlates positively with β_{1500} in our NIRCam sample with slope $= 0.49$ and the Spearman correlation coefficient $= 0.32$. Similarly, $\xi_{\rm ion}$ correlates positively with β_{1500} with slope of 0.5 in out NIRSpec sample. However, the β_{1500} measurement from EAZY SED fitting recovers β_{1500} in a small range ($-3.1 < \beta_{1500} < 2$), and we find a significant scatter of $\xi_{\rm ion}$ within this range. Compared to other studies, Bouwens et al. (2016) and Castellano et al. (2023) find a negative correlation of β_{1500} with $\xi_{\rm ion}$, whereas Lam et al. (2019) find no significant correlation. From the variability of β_{1500} with measurement and the difference in results across literature, we infer that $\xi_{\rm ion}$ is not correlated with β_{1500} at $z > 5$.

We measure the correlation between $\xi_{\rm ion}$ and the $M_{\rm UV}$. We find a positive correlation with a slope and Spearman correlation coefficients of 0.16 and 0.34 in our NIRCam sample, and 0.18 and 0.61 in our NIRspec sample. We find a steeper correlation between $\xi_{\rm ion}$ and $M_{\rm UV}$ compared to Bouwens et al. (2016), Castellano et al. (2023), and Lam et al. (2019). We are able to increase the range of $M_{\rm UV}$ towards the faint end to ~ -16 and our result indicates a higher production rate of ionizing photons for UV faint galaxies compared to other studies.

4.3 Ionization conditions from rest-frame emission lines

The ionizing photon production efficiency depends on the star formation and the ionizing conditions of the galaxy ISM. In this section, we study the correlation between $\xi_{\rm ion}$ and Hα and [O III](+ Hβ) EWs which trace the average stellar ages and the ionization parameter of the ISM respectively. Fig. 9 shows $\xi_{\rm ion}$ as a function of Hα EW (left) and [O III](+ Hβ) EW (right). $\xi_{\rm ion}$ is highly correlated with Hα EW in both NIRCam (slope 0.7, Spearman coefficient 0.6) and NIRSpec (slope 0.5, Spearman coefficient 0.5) samples. Although partially the correlation found is driven by the fact that $\xi_{\rm ion}$ is measured with Hα luminosity, $\xi_{\rm ion}$ is also dependent on UV luminosity, and Hα EW is dependent on the strength of the stellar continuum as well. Our results are comparable with Atek et al. (2022), who find a correlation with a slope of 0.63 for low stellar mass galaxies at $z\sim 1$ and other studies at low redshifts ($z\sim 1-2$, Emami et al. 2020; Tang et al. 2019; Matthee et al. 2017).

At lower redshifts ($z\sim 1-2$), $\xi_{\rm ion}$ is known to correlate with the [O III] + Hβ EW (Chevallard et al. 2018; Tang et al. 2019; Onodera et al. 2020). At higher redshifts, Tang et al. (2023) show for a small

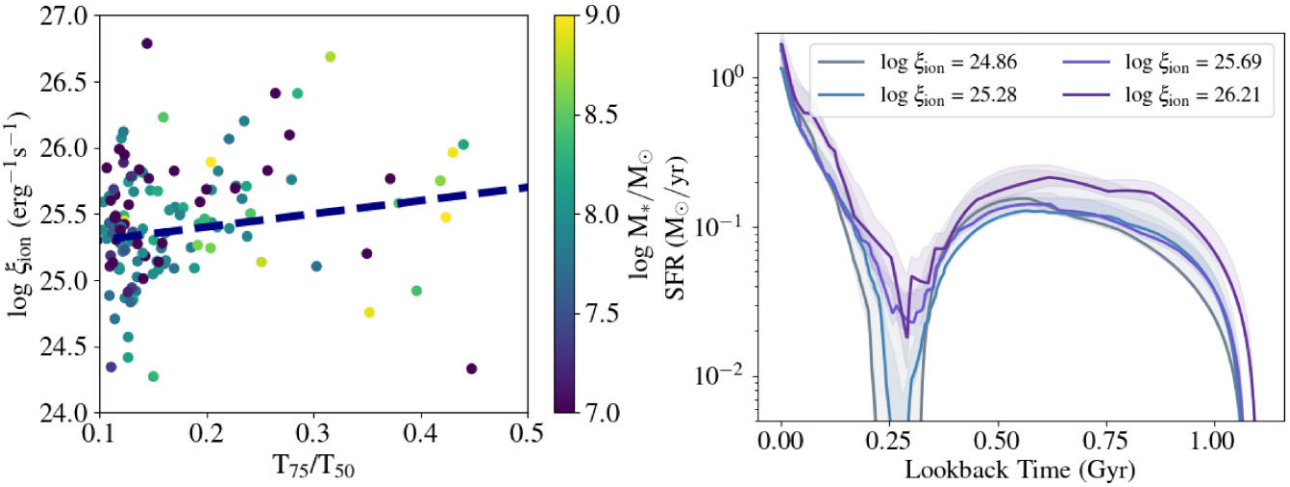

Figure 7. The ionizing photon production efficiency ($\xi_{\rm ion}$) is slightly positively correlated with T_{75}/T_{50} (left). A more recent burst in star formation has a smaller T_{75}/T_{50}. The markers have been colour-coded with the magnification-corrected stellar mass of the galaxy. The right panel shows the SFH of galaxies in bins of $\xi_{\rm ion}$ with median $\xi_{\rm ion}$ of the bin stated in the legend.

[!h]

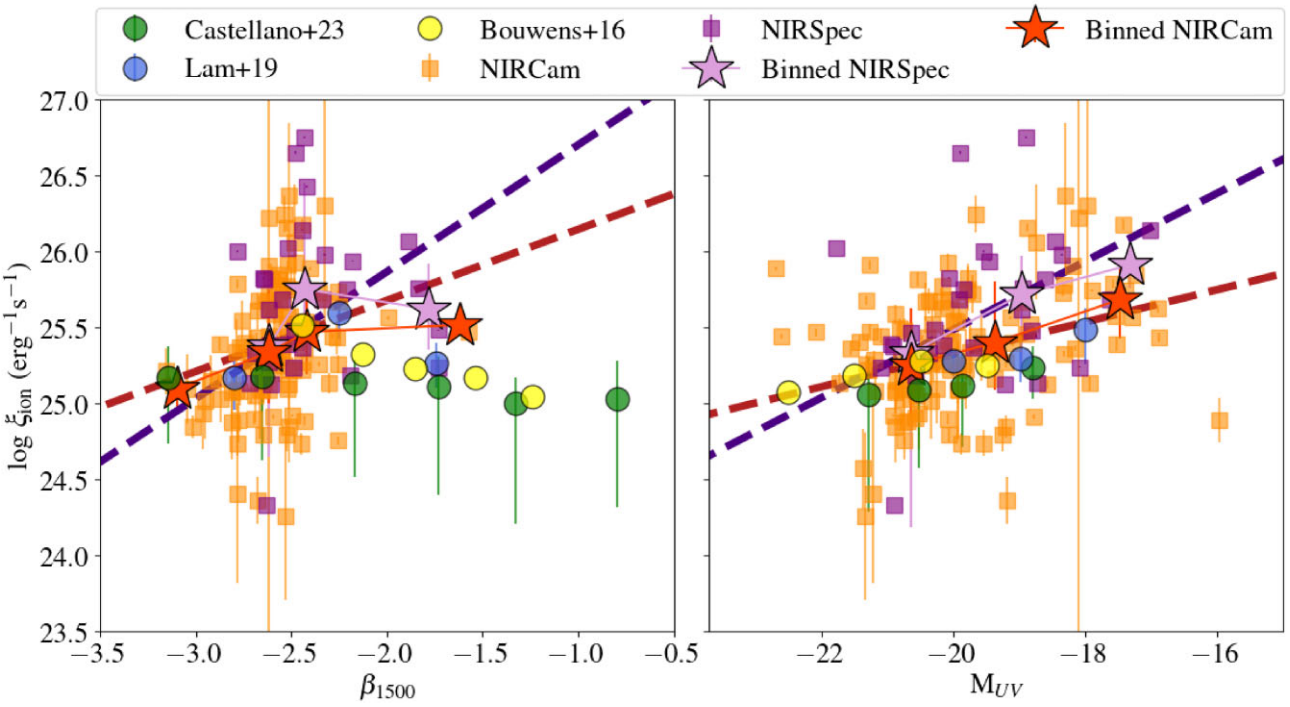

Figure 8. The ionizing photon production efficiency ($\xi_{\rm ion}$) as a function of UV slope (β_{1500}) (left) and the UV magnitude ($M_{\rm UV}$) (right). The purple and orange colours show the NIRSpec and NIRCam samples, respectively. The squares and stars show individual galaxies and binned samples with the lines showing linear fits to the sample. We find a positive correlation of $\xi_{\rm ion}$ with the $M_{\rm UV}$ in both NIRCam and NIRSpec samples similar to past studies. However, we find no significant correlation between $\xi_{\rm ion}$ and β_{1500}.

sample of $z > 7$ galaxies that the $\xi_{\rm ion}$ is similarly correlated with [O III] + Hβ EW and also that [O III] + Hβ EW is correlated with the O32 ratio which traces the ionization parameter of the galaxy ISM. Here, we investigate the correlation of $\xi_{\rm ion}$ [O III](+ Hβ) EW in our NIRSpec and NIRCam (only in the NCF field) samples. We find that, $\xi_{\rm ion}$ is moderately correlated with [O III] + Hβ EW in the NIRCam sample (slope 0.12, Spearman coefficient 0.5) and with [O III] EW in the NIRSpec sample (slope 0.4, Spearman coefficient 0.3). This result is consistent with the correlation found in both lower and higher redshift samples (Chevallard et al. 2018; Tang et al. 2019, 2023; Onodera et al. 2020). In conjunction with the result in Tang et al. (2023), this indicates that $\xi_{\rm ion}$ is correlated with the ionization parameter of the galaxy.

In the NIRCam sample, we find median [O III] + Hβ EW = 1861 ± 433 Å which is comparable to 1993 ± 214 Å for [O III] emitters at $z\sim$ 8 (Tang et al. 2023) but higher than the ∼ 700 Å at $z\sim$ 6 found in Endsley et al. (2023a). The higher [O III] + Hβ EW in our sample compared to Endsley et al. (2023a) could be driven by our

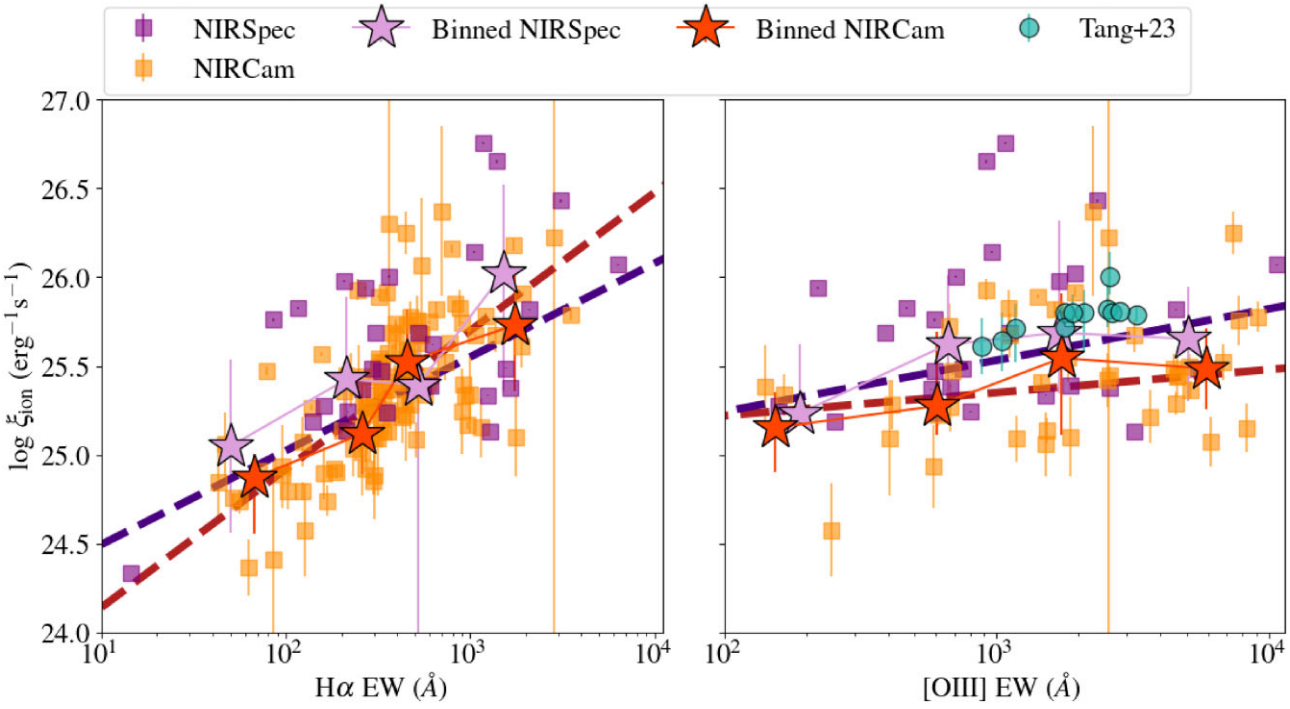

Figure 9. The ionizing photon production efficiency (ξ_{ion}) as a function of Hα EW (left) and [O III] EW (right). The purple and orange colours show our NIRSpec and NIRCam samples, respectively. The [O III] EW is only shown for the galaxies in the NCF field which have medium band observation of 5007 Å rest-frame wavelength. The squares and stars show individual galaxies and binned samples with the lines showing linear fits to the sample. We find a positive correlation of ξ_{ion} with the Hα EW. We also find a moderate positive correlation of ξ_{ion} with the [O III] EW.

Hα selection which biases the sample towards higher star forming and hence emission-line galaxies. In our NIRSpec sample, we find a median [O III] EW of 802 ± 360 Å which is higher compared to the lower redshift sample ($\sim$100 Å for star-forming galaxies at z= 2, Reddy et al. 2018), but similar to the [O III] EWs in extreme emission-line galaxies at $z\sim$ 3 (Gupta et al. 2023).

Further, we investigate the correlation of Hα and [O III] + Hβ EWs with the UV magnitude shown in Fig. 10. We find a positive correlation between Hα and the M_{UV} in the NIRCam sample with a slope of 0.12 and a Spearman correlation coefficient of 0.41 with a very small p-value indicating a strong correlation. However, we find no significant correlation between Hα and the M_{UV} in the NIRSpec sample with 0 slope and a large p-value for the Spearman correlation coefficient. The difference in correlation of Hα with M_{UV} between the NIRSpec and NIRCam sample might be driven by the Hα selection and shallower depth of the NIRSpec sample compared to the NIRCam sample. We note that at $M_{UV} < -18$, we also find a large scatter in Hα (median Hα EW = 339.27 Å and σ = 1651.06 Å) compared to the fainter end ($M_{UV} > -18$; median Hα EW = 517.8 Å and σ = 794.69 Å). Although the UV faint sample ($M_{UV} > -18$) has been magnified due to gravitational lensing from the foreground cluster, Hα EW is independent of the magnification. Our results are comparable to the median Hα EW ($\approx$ 400 Å) found in previous studies (Faisst et al. 2019; Lam et al. 2019). However, we report a lower median Hα EW compared to EW reported in Endsley et al. (2023b), who also do not find a correlation between Hα EW and M_{UV} in the Lyman-break-selected galaxies.

Fig. 10 shows the correlation between [O III] + Hβ EW and the UV magnitude. We find no significant correlation between [O III] + Hβ EW in the bright UV sample ($M_{UV} < -18$). Due to the lack of medium-band observations of the [O III] + Hβ emission in the CLU field which are magnified due to gravitational lensing, we are limited to the $M_{UV} < -18$ sample. Within the range $-23 < M_{UV} < -18$, we find a median [O III] + Hβ EW = 917.27 Å and a large scatter of σ = 2621.65 Å. We also do not find a correlation between [O III] + Hβ EW and the UV magnitude with 0 slope and large p-value for Spearman correlation coefficients. Similar to previous studies, we find a large [O III] + Hβ EW compared to $z\sim$ 2, and 46 extreme emission galaxies with > 1200 Å [O III] + Hβ EW. The median [O III] + Hβ EW of our NIRCam sample is lower than 1994 Å reported in Tang et al. (2023) for $z>$ 7 galaxies but higher than median [O III] + Hβ EW ($< 890 \pm 60$ Å) reported in Endsley et al. (2023b). Endsley et al. (2023b) also find that the UV faint ($M_{UV} > -19$) galaxies have a lower [O III] + Hβ EW which is driven by lower metallicities as well as more recently declining SFHs relative. However, in our sample, we find that the UV faint ($M_{UV} > -19$) galaxies have a higher Hα EW which indicates lower metallicities and high SFRs. The difference in trends compared to Endsley et al. (2023b) could arise from differences in sample selection strategies, where we have selected galaxies with *F410M* band excess that biases our sample towards star forming galaxies with higher nebular emission, whereas Endsley et al. (2023b) follow a Lyman-break selection which allows them to select galaxies that are not biased towards higher emission.

5 CONCLUSIONS

In this work, we present the UV and ionization properties and star formation of dwarf galaxies at $z\sim$ 5–7. We use the CANUCS NIRCam and NIRSpec observations of the MACS0417 CLU field and the respective NCF field. Our sample is selected with a *F410M* band flux excess at $4.8 < z < 5.5$ such that the Hα emission is included in the medium band and we can measure accurate emission-

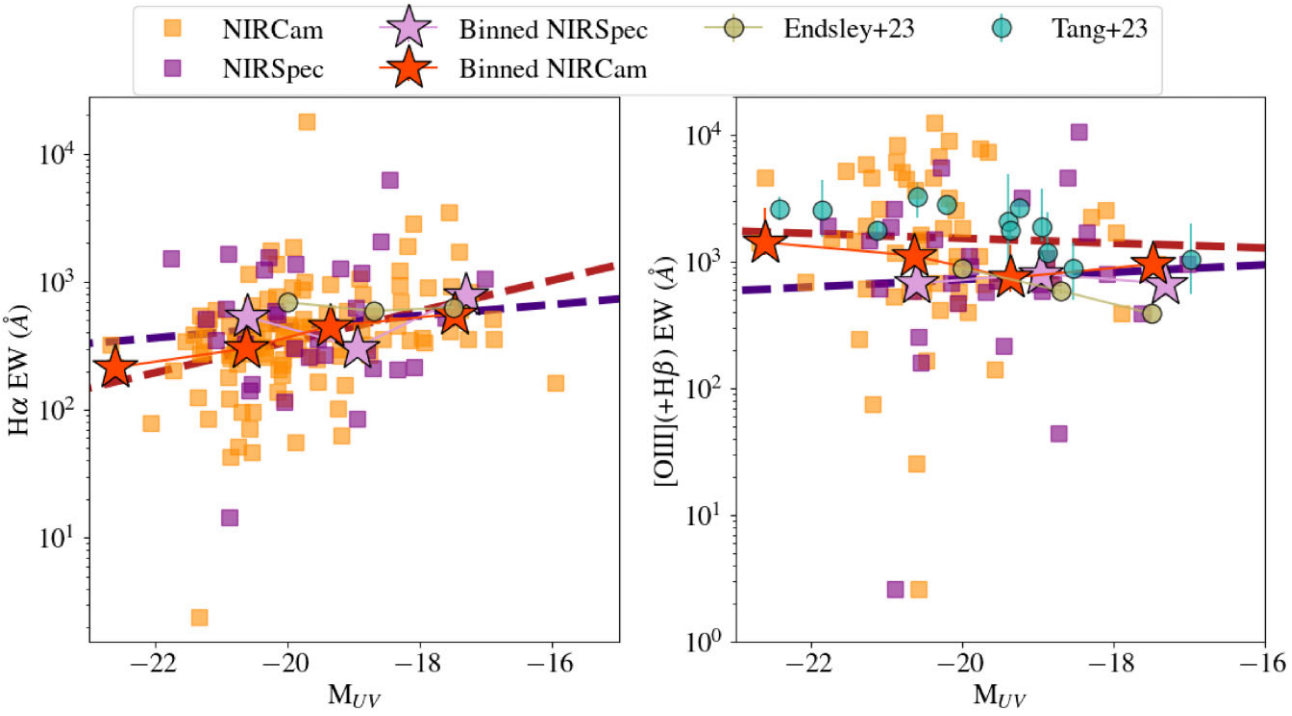

Figure 10. Hα EW (left) and [O III](+ Hβ) EWs (right) as a function of UV magnitude. The purple and orange colours show our NIRSpec and NIRCam samples, respectively. The [O III] EW is shown for the NIRSpec sample and [O III] + Hβ EW for galaxies in the NCF field which have medium-band observation of 5007 Å rest-frame wavelength. The squares and stars show individual galaxies and binned samples with the lines showing linear fits to the sample. We find a positive correlation of Hα EW with the UV magnitude and no significant correlation of [O III](+ Hβ) EW with the UV magnitude.

line flux and EWs. We confirm the line fluxes for a subset of the NIRCam sample with NIRSpec follow-up (Fig. 2). With the magnification from the foreground cluster scale lens in our field, we are also able to push to fainter and lower mass galaxies compared to previous studies at similar redshifts. Using this data, we discussed the evolution of β_{1500} and $\xi_{\rm ion}$, and their dependence on the galaxy properties and SFHs. We also study the ionizing properties of our sample using emission-line EWs. We summarize our results as follows:

1. We find bluer UV slopes of dwarf galaxies with median β_{1500} -2.56 ± 0.26 in the NIRCam sample. We find no significant evolution of β_{1500} with redshift during the EoR but find a significant correlation between β_{1500} and the stellar mass of the galaxy in both our sample sets. These results indicate a lack of dust build-up or a higher presence of ionizing radiation in star-forming dwarf galaxies at $z\sim$ 5.

2. We do not find any evolution of $\xi_{\rm ion}$ with redshift in the EoR and no significant difference between $\xi_{\rm ion}$ of LAEs reported in the literature with our sample (median $\log\xi_{\rm ion} = 25.36 \pm 0.04$ and 25.49 ± 0.18 in NIRCam and NIRSpec samples, respectively, Fig. 5). The median $\log\xi_{\rm ion}$ of our sample sets is also above the canonical value of 25.2 required to reionize the local IGM with approximately 20 per cent escape fraction (Robertson et al. 2015). The lack of difference between the median $\xi_{\rm ion}$ LAEs and non-emitters indicates different physical processes affecting the production of ionizing photons and the creation of escape channels for Lyman-α photons.

3. We find a moderate correlation of $\xi_{\rm ion}$ with the stellar mass and the sSFRs in a galaxy, such that $\xi_{\rm ion}$ decreases with increasing stellar mass and increases with increasing sSFR (Fig. 6). On further investigation of the SFHs, we find that the majority of our Hα selected galaxies are undergoing recent star formation raise/burst which creates a large scatter in the $\xi_{\rm ion}$. We also find that the relative time of burst is correlated to average $\xi_{\rm ion}$ and indicates a delay in of $\approx$ 50 Myr between the final rise in star formation/burst and increasing $\xi_{\rm ion}$ (Fig. 7).

4. We investigate the correlation between $\xi_{\rm ion}$ and UV properties β_{1500} and $M_{\rm UV}$. We find a significant correlation between $M_{\rm UV}$ and $\xi_{\rm ion}$, such that $\xi_{\rm ion}$ increases with decreasing $M_{\rm UV}$. This implies a possible greater contribution of UV faint and dwarf galaxies to reionizing the Universe. However, we find no significant and opposite correlation between β_{1500} and $\xi_{\rm ion}$. The NIRCam sample, which covers a small dynamic range of beta finds higher $\xi_{\rm ion}$ for redder β_{1500}. The large scatter in β_{1500} and $\xi_{\rm ion}$, which arise due to the stochastic nature of SFHs in dwarf galaxies could explain the observed discrepancy.

5. We also find a significant correlation between $\xi_{\rm ion}$ and EWs of rest-frame optical emission lines. We find that $\xi_{\rm ion}$ cincreases highly with increasing Hα EW and moderately with [O III] + Hβ EW. We further explore the correlation of rest-frame optical emission EWs with $M_{\rm UV}$. We find that on average Hα EW increases with $M_{\rm UV}$, although our bright end of the $M_{\rm UV}$ range has a high scatter in Hα EW indicating a stochastic SFH with very recent bursts. However, our UV faint sample shows a high Hα EW. On the other hand, we do not find a significant correlation between [O III] + Hβ EW and $M_{\rm UV}$. However, the lack of medium band observation covering the [O III] + Hβ emission in the CLU field limits us to $M_{\rm UV} < -18$, where we similarly find a large scatter in [O III] + Hβ EW.

Our results from one of the five cluster fields of CANCUS provide a large set of empirical measurements of UV and ionizing properties of dwarf star-forming galaxies at $z>$ 5. We demonstrate here the use of medium-band photometry to accurately derive emission-line fluxes without having to rely solely on spectroscopy. Similar

studies characterizing the properties of dwarf galaxies across the EoR are required to fully understand how reionization of the Universe progressed. This work will be supplemented by future studies with the full CANUCS data at $z > 5$, which will provide a better understanding of the general population of galaxies across the history of the Universe.

ACKNOWLEDGEMENTS

AH, MB, GR, and NM acknowledge support from the ERC Grant FIRSTLIGHT and Slovenian National Research agency ARRS through grants N1-0238 and P1-0188. MB acknowledges support from the program HST-GO-16667, provided through a grant from the STScI under NASA contract NAS5-26555. This research was enabled by grant 18JWST-GTO1 from the Canadian Space Agency and funding from the Natural Sciences and Engineering Research Council of Canada. This research used the Canadian Advanced Network For Astronomy Research (CANFAR) operated in partnership by the Canadian Astronomy Data Centre and The Digital Research Alliance of Canada with support from the National Research Council of Canada the Canadian Space Agency, CANARIE and the Canadian Foundation for Innovation. The Cosmic Dawn Center (DAWN) is funded by the Danish National Research Foundation under grant no. 140.

DATA AVAILABILITY

Raw *JWST* data used in this work are available from the Mikulski Archive for Space Telescopes (https://archive.stsci.edu; doi: 10.17909/ph4n-6n76). Processed data products will be available on http://canucs-jwst.com.

REFERENCES

Alcorn L. Y. et al., 2019, ApJ, 883, 153
Anderson L., Governato F., Karcher M., Quinn T., Wadsley J., 2017, MNRAS, 468, 4077
Asada Y. et al., 2024, MNRAS, 527, 11372
Atek H., Richard J., Kneib J. P., Schaerer D., 2018, MNRAS, 479, 5184
Atek H., Furtak L. J., Oesch P., Dokkum P. V., Reddy N., Contini T., Illingworth G., Wilkins S., 2022, MNRAS, 511, 4464
Atek H. et al. , 2023.
Balu S., Greig B., Qiu Y., Power C., Qin Y., Mutch S., Wyithe J. S. B., 2023, MNRAS, 520, 3368
Bhatawdekar R., Conselice C. J., Margalef-Bentabol B., Duncan K., 2019, MNRAS, 486, 3805
Bolan P. et al., 2022, MNRAS, 517, 3263
Bouwens R. J. et al., 2012, ApJ, 752, L5
Bouwens R. J. et al., 2015a, ApJ, 803, 34
Bouwens R. J., Illingworth G. D., Oesch P. A., Caruana J., Holwerda B., Smit R., Wilkins S., 2015b, ApJ, 811, 140
Bouwens R. J., Smit R., Labbé I., Franx M., Caruana J., Oesch P., Stefanon M., Rasappu N., 2016, ApJ, 831, 176
Bradley L. et al. , 2022, astropy/photutils: 1.6.0. Zenodo
Brammer G., 2023a, eazy-py. Zenodo
Brammer G., 2023b, msaexp: NIRSpec analyis tools. Zenodo
Brammer G., Matharu J., , 2021, gbrammer/grizli: Release 2021. Zenodo
Brammer G. B., van Dokkum P. G., Coppi P., 2008, ApJ, 686, 1503
Byler N., 2018, nell-byler/cloudyfsps: Initial release of cloudyFSPS. Zenodo
Calzetti D., Kinney A. L., Storchi-Bergmann T., 1994, ApJ, 429, 582
Calzetti D., Armus L., Bohlin R. C., Kinney A. L., Koornneef J., Storchi-Bergmann Th., 2000, ApJ, 533, 682
Cameron A. J. et al., 2023, A&A, 677, A115
Castellano M. et al., 2023, A&A, 675, A121
Chabrier G., 2003, PASP, 115, 763
Chevallard J. et al., 2018, MNRAS, 479, 3264
Chisholm J. et al., 2022, MNRAS, 517, 5104
Coil A. L. et al., 2015, ApJ, 801, 35
Conroy C., Gunn J. E., 2010, Astrophysics Source Code Library, record ascl:1010.043
Davies F. B. et al., 2018, ApJ, 864, 142
Dressler A., Henry A., Martin C. L., Sawicki M., McCarthy P., Villaneuva E., 2015, ApJ, 806, 19
Duncan K., Conselice C. J., 2015, MNRAS, 451, 2030
Eisenstein D. J. et al. , 2023, preprint (arXiv:2306.02465)
Eldridge J. J. et al., 2017, Publ. Astron. Soc. Aust., 34, e058
Emami N., Siana B., Alavi A., Gburek T., Freeman W. R., Richard J., Weisz D. R., Stark D. P., 2020, ApJ, 895, 116
Endsley R. et al. , 2023a.
Endsley R. et al. , 2023b.
Erb D. K., 2015, Nature, 523, 169
Faisst A. L., Capak P. L., Emami N., Tacchella S., Larson K. L., 2019, ApJ, 884, 133
Ferland G. J. et al. , 2017.
Finkelstein S. L. et al., 2015, ApJ, 810, 71
Finkelstein S. L. et al., 2019, ApJ, 879, 36
Gupta A. et al., 2023, MNRAS, 519, 980
Ishigaki M., Kawamata R., Ouchi M., Oguri M., Shimasaku K., Ono Y., 2015, ApJ, 799, 12
Iyer K., Gawiser E., 2017, ApJ, 838, 127
Iyer K. G., Gawiser E., Faber S. M., Ferguson H. C., Kartaltepe J., Koekemoer A. M., Pacifici C., Somerville R. S., 2019, ApJ, 879, 116
Jiang L., Cohen S. H., Windhorst R. A., Egami E., Finlator K., Schaerer D., Sun F., 2020, ApJ, 889, 90
Jullo E., Kneib J. P., Limousin M., Elíasdóttir Á., Marshall P. J., Verdugo T., 2007, New J. Phys., 9, 447
Karman W. et al., 2017, A&A, 599, A28
Kneib J. P., Mellier Y., Fort B., Mathez G., 1993, A&A, 273, 367
Lam D. et al., 2019, A&A, 627, A164
Larson R. L. et al. , 2022.
Leitherer C., Heckman T. M., 1995, ApJS, 96, 9
Lin Y.-H. et al. , 2023.
Livermore R. C., Finkelstein S. L., Lotz J. M., 2017, ApJ, 835, 113
Mahler G. et al., 2019, ApJ, 873, 96
Markov V., Gallerani S., Ferrara A., Pallottini A., Parlanti E., Di Mascia F., Sommovigo L., Kohandel M., , 2024, preprint (arXiv:2402.05996)
Mascia S. et al. , 2023.
Matthee J., Sobral D., Best P., Khostovan A. A., Oteo I., Bouwens R., Röttgering H., 2017, MNRAS, 465, 3637
Matthee J., Mackenzie R., Simcoe R. A., Kashino D., Lilly S. J., Bordoloi R., Eilers A.-C., 2023, ApJ, 950, 67
McGreer I., Mesinger A., D'Odorico V., 2015, MNRAS, 447, 499
Mehta V. et al., 2017, ApJ, 838, 29
Naidu R. P., Tacchella S., Mason C. A., Bose S., Oesch P. A., Conroy C., 2020, ApJ, 892, 109
Nakajima K., Ellis R. S., Iwata I., Inoue A. K., Kusakabe H., Ouchi M., Robertson B. E., 2016, ApJ, 831, L9
Nanayakkara T. et al., 2020, ApJ, 889, 180
Nanayakkara T. et al., 2023, ApJ, 947, L26
Ning Y., Cai Z., Jiang L., Lin X., Fu S., Spinoso D., 2023, ApJ, 944, L1
Noirot G. et al., 2023, MNRAS, 525, 1867
Onodera M. et al., 2020, ApJ, 904, 180
Osterbrock D. E., 1989, Astrophysics of Gaseous Nebulae and Active Galactic Nuclei. University Science Books, Mill Valley, CA
Ouchi M. et al., 2009, ApJ, 706, 1136
Paardekooper J.-P., Khochfar S., Vecchia C. D., 2013, MNRAS, 429, L94
Prieto-Lyon G. et al., 2023, A&A, 672, A186
Reddy N. A., Steidel C. C., 2009, ApJ, 692, 778
Reddy N. A. et al., 2018, ApJ, 869, 92
Robertson B. E., 2022, ARA&A, 60, 121
Robertson B. E., Ellis R. S., Furlanetto S. R., Dunlop J. S., 2015, ApJ, 802, L19

Sawicki M., Thompson D., 2006, ApJ, 648, 299
Saxena A. et al. , 2023.
Simmonds C. et al. , 2023.
Stefanon M. et al., 2019, ApJ, 883, 99
Stefanon M., Bouwens R. J., Illingworth G. D., Labbé I., Oesch P. A., Gonzalez V., 2022, ApJ, 935, 94
Tang M., Stark D. P., Chevallard J., Charlot S., 2019, MNRAS, 489, 2572
Tang M. et al. , 2023.
Topping M. W. et al. , 2023.
Vilella-Rojo G. et al., 2015, A&A, 580, A47
Willott C. J. et al., 2022, PASP, 134, 025002
Wise J. H., Demchenko V. G., Halicek M. T., Norman M. L., Turk M. J., Abel T., Smith B. D., 2014, MNRAS, 442, 2560
Yamanaka S., Yamada T., 2019, PASJ, 71, 51

This paper has been typeset from a TEX/LATEX file prepared by the author.